Applied Catalysis B: Environmental 340 (2024) 123182

Contents lists available at ScienceDirect

Applied Catalysis B: Environmental

journal homepage: www.elsevier.com/locate/apcatb

Localized ultrafine Cu clusters within MOF-derived metal oxides for collective photochemical and photothermal H_2 generation

Serene Wen Ling Ng [a,1], Kane Jian Hong Lim [a,1], Minmin Gao [a], Wanheng Lu [a], Tanmay Ghosh [b], Mingsheng Zhang [b], Sibudjing Kawi [c], Minghui Hong [a,d,*], Ghim Wei Ho [a,**]

[a] Department of Electrical and Computer Engineering, National University of Singapore, 4 Engineering Drive 3, Singapore 117583, Republic of Singapore
[b] Institute of Materials Research and Engineering (IMRE), Agency for Science, Technology and Research (A*STAR), 2 Fusionopolis Way, Innovis #08-03, Singapore 138634, Republic of Singapore
[c] Department of Chemical & Biomolecular Engineering, National University of Singapore, 4 Engineering Drive 4, 117585 Republic of Singapore
[d] Pen-Tung Sah Institute of Micro-Nano Science and Technology, Xiamen University, 33 Qunxian Road, Xiamen 361005, China

ARTICLE INFO

Keywords:
Ultrafine metal clusters
Hierarchical pore structure
Photochemical
Photothermal
Photocatalytic H_2 generation

ABSTRACT

The ability to prepare ultrafine metal cluster (UMC) in supported catalysts, which exhibit extraordinary physical and chemical properties offers exciting opportunities to tailoring catalytic performance. However, the fabrication of singly-dispersed metal cluster catalysts that are both catalytic stable and active remains challenging. In this work, ultrafine Cu clusters has been spatially immobilized within the MOF derived photocatalyst matrix to realize a unitary photocatalyst with high density and stable active sites for charge separation and photothermal co-functions. Furthermore, the embedded Cu is capable of overcoming challenges related to porous structure collapse, disparate material interfaces and incompatibility between light absorption and charge transfer processes. Resultantly, the photocatalyst (m-TiO_2/Cu) exhibits a high and stable H_2 generation rate of 17.8 $mmolg^{-1}h^{-1}$ that is ~69 times higher compared to the control. In essence, this study presents an efficient approach to immobilize ultrafine metal active sites for the development of high-performance heterogeneous catalysts for energy applications.

1. Introduction

Solar to chemical energy conversion has been recognized for reducing the reliance on non-renewable fossil fuels. This led to increasing attention towards photocatalytic H_2 generation as a green alternative path for energy production [1–6]. Recently, there has been growing interest in ultrafine or finely dispersed embedded catalysts due to optimal catalyst utilization, small size effect, high intrinsic activity, and favorable support interactions, all of which contribute to enhanced catalytic performance [7–12]. However, the inherent high surface energy of ultrafine metal clusters (UMC) poses a challenge as they are thermodynamically unstable and susceptible to aggregation during catalytic reactions, leading to poor catalytic activity [3,13,14]. One conventional approach to achieve well-dispersed UMC is the colloidal method [15–18]. However, the presence of capping agents used in this method [19] introduces contaminants that adversely affect catalytic performance, and the removal of these agents may undesirably result in particle agglomeration.[20,21] Despite extensive research, the development of methods capable of producing stably dispersed UMC remains limited. To overcome the limitations of unsupported metal particles, the utilization of highly supported metal-organic frameworks (MOFs) with hierarchical pores are adopted for a controlled preparation of UMC [22–26]. By employing MOFs as a host, guest UMC can be localized within their well-defined pores to prevent aggregation and leaching of nanoparticles [22–24,27]. The modified pore structure, accompanied by an inherently high surface area of MOF also eases the uniform dispersion of metal precursor which can be anchored to metal sites or organic linkers of the MOF, preventing further aggregation during the chemical and morphological transformation process of MOF-derived materials [28–31].

* Corresponding author at: Department of Electrical and Computer Engineering, National University of Singapore, 4 Engineering Drive 3, Singapore 117583, Republic of Singapore.
** Corresponding author.
E-mail addresses: elehmh@nus.edu.sg (M. Hong), elehgw@nus.edu.sg (G.W. Ho).
[1] These authors contributed equally to this work.

https://doi.org/10.1016/j.apcatb.2023.123182
Received 19 May 2023; Received in revised form 14 July 2023; Accepted 16 August 2023
Available online 17 August 2023

The flexibility and simplicity of converting MOFs to MOF-derived photocatalytic active materials such as oxides, sulfides, and phosphides, makes it a favorable approach for porous catalyst design [32–37]. This not only resolves the instability drawbacks of pristine MOF, but also retains the structural advantages of MOF photocatalyst and allows the incorporation of UMC for photochemical and/or photothermal enhancement. In the context of designing photothermal catalyst, it is imperative for solar absorbers to possess the ability to generate heat in a localized manner, specifically in close proximity to the photocatalyst [38]. Furthermore, achieving optimal charge separation necessitates the co-catalyst to be also localized within the photocatalyst matrix. However, this presents a dilemma in conventional photocatalyst systems with extended light absorption, as there is an inevitable trade-off between maximizing light harvesting to sustain high photoredox activity and ensuring effective photothermal heating capability [39]. Moreover, from the perspective of collegial photothermal catalyst design, it is essential that solar absorbers do not disrupt the charge transfer pathway of the photocatalyst and the co-catalyst. Essentially, achieving optimal performance in photocatalysis by fully utilizing the entire solar spectrum through synergetic structure engineering, enhanced charge transfer dynamics and photothermal effects remains particularly challenging. In this aspect, the utilization of a multi-functional UMC locally immobilized within the photocatalyst capable of supporting this trichotomous role holds great promise in fulfilling demanding photothermal catalysts design.

Herein, this work presents the spatial immobilization of ultrafine Cu clusters within the MOF derived photocatalyst matrix that results in a unitary photocatalyst with high density and stable active sites for charge separation and photothermal co-functions. The proposed in-situ MOF immobilized UMC, not only circumvents disparate material interfacial issues but also mitigate overlapped light absorption and disrupted charge transfer incompatibilities. Specifically, the hierarchical porous TiO_2 nanosheets are achieved by modifying the synthesis of classical Ti-MOF (MIL-125), enabling high energy photon (UV) photoredox reaction. Taking advantage of mesopores and macropores of the modified MOF (m-MOF), infiltrated Cu precursor manifests complete inclusion within the pores of the m-MOF to serve as a coordinated reinforcement to prevent structural collapse of the m-MOF. Additionally, the embedded Cu exists as ultrafine clusters with narrow size distribution, maximizing surface atoms utilization efficiency and improving charge transport due to shortened charge diffusion distance. Notably, the localized surface plasmon resonance (LSPR) observed in Cu clusters becomes prominent, which is key to achieving highly localized photothermal induced near-field temperature rise in close proximity to the catalyst–reactant complexes. To the best of our knowledge, this is the first reported instance of single metal, Cu clusters locally dispersed and embedded in MOF derived nanosheets to fulfill dual photochemical and photothermal roles. The photocatalyst (m-TiO_2/Cu) exhibited a high and stable H_2 production rate of 17.8 mmol g^{-1} h^{-1}, which has an enhancement of ~69 times compared to the control sample (TiO_2). These findings introduce an efficient pathway to immobilize and tailor ultrafine metal active sites to realize high performance heterogeneous catalysts for energy and environmental applications.

2. Experimental sections

2.1. Synthesis of MIL-125 and m-MIL-125 derived TiO_2 (TiO_2 and m-TiO_2 respectively)

35 ml of DMF (Dimethylforamide) was added to 5 ml of methanol in a 100 ml Teflon vessel. Next, 2.5 g of H_2BDC (Terephthalic acid) and 1 ml of TTIP (Titanium Isopropoxide) was added to the above solution. The solution was left to stir for 1 min. The Teflon vessel was then placed in an autoclave and left in the oven at 150 °C for 20 h. The final product was obtained by washing with methanol and DMF alternatively for three times and dried in the oven at 60 °C. The samples were annealed at 450 °C for 4 h at a ramp rate of 2 °C per min. This product was labelled as TiO_2. Next, m-TiO_2 was synthesized using a similar method as above but with 20 ml of DMF, 20 ml of methanol, 1.5 g of H_2BDC and 1 ml of TTIP.

2.2. Synthesis of m-TiO_2/Cu

The as-prepared m-MIL-125 was dispersed in 2 ml of water. Next, different amount of Copper Acetate (1 wt%, 3 wt%, 4.5 wt% and 6.0 wt %) were added to the above solution. The solutions were left to stir for 1 min and then dried in the freeze dryer for 24 h. After freeze drying, the samples were annealed at 450 °C for 4 h at a ramp rate of 2 °C per min.

2.3. Synthesis of m-TiO_2/Cu-C

The as-prepared m-TiO_2 was dispersed in 2 ml of DI water. Next, Cu amount of 4.5 wt% using Copper Acetate as the Cu precursor was added to the above solution. The samples were dried in the crucible at 40 °C and then annealed at 250 °C for 30 min at a ramp rate of 2 °C per min.

2.4. Materials characterizations

The Scanning Electron Microscope (SEM) characterization was carried out using a JEOL FEG JSM 7001F with field-emission operating at 15 kV. Transmission Electron Microscopy (TEM) and TEM-EDX were performed using Titan 80–300 keV and Tecnai G2 80–200 keV, respectively (Thermo Fisher Scientific, Waltham, MA USA). XRD spectra were obtained using X-ray diffraction (XRD, 5005 Bruker X-ray diffractometer equipped with graphite-monochromated Cu Kα radiation at $\lambda = 1.54$ Å). Absorption spectra were measured using a Shimadzu UV-3600 UV–vis–NIR spectrophotometer. Atomic Force Microscopy (AFM) and Kelvin Probe Force Microscopy (KPFM) equipped with light sources of different wavelengths were utilized to examine samples' morphology and changes in the contact potential difference (CPD) caused by light illumination. For KPFM, a double-passing scheme with a lift height of 40 nm was adopted to minimize the crosstalk of topography to potential signals. Both AFM and KPFM measurements were carried out on a commercial Scanning Probe Microscopy (SPM) system (MPF-3D, Asylum Research, Oxford Instruments, USA) and conductive Pt-coated silicon tips with a spring constant of 2 N/m and a tip radius of ~ 15 nm (AC240-PP, Olympus, Japan) were used. Brunauer–Emmett–Teller (BET) measurements were measured using Quantachrome Nova 2200e with N_2 as the adsorbate at liquid nitrogen temperature. Photoluminescence (PL) and transient measurements were measured using a Horiba Fluorolog-3 spectrofluorometer. Infrared images and temperature profile measurements of the dry powdered samples were captured using a FLIR E50 infrared (IR) camera. The XPS was performed using AXIS Supra+ (Shimadzu, Kratos). The C 1 s peak at 284.8 eV is used as the internal reference value to revise the surface charging effects.

2.5. Photocatalytic H_2 generation measurements

The H_2 generation measurements were performed in a quartz vial using 1 mg of photocatalyst in 10 ml of aqueous 30 wt% methanol solution. The quartz vial was purged with Ar gas for 10 min before the measurements and irradiated with a UV LED (365 nm) with light intensity of 150 mW cm^{-2}. The visible-NIR light source used is a Xenon lamp (Excelitas, PE300BFM) equipped with a 400 nm long-pass filter and with light intensity of 100 mW cm^{-2}. For full spectrum measurements, both of these light sources were used in tandem. The reactor was syringed drawn (100 μl) to measure the H_2 gas amount using gas chromatography (Shimadzu, GC-2014AT).

2.6. Photocurrent measurements

Samples for photocurrent measurements were prepared on fluorine doped tin oxide (FTO) coated glass, by drop-casting method. Solutions

were prepared using m-TiO_2 or m-TiO_2/Cu samples together with 0.99 ml ethanol and 0.01 ml Nafion. The mixed solutions were then dripped on the surface of the FTO glass and dried at 60 °C. The photocurrent measurements were carried out with an electrochemical workstation (CHI-660E) with 2 electrode configuration, using the prepared sample on FTO as photoanode and Pt as a counter electrode at zero bias in 0.5 M Na_2SO_4 aqueous solution. The photocurrent measurements were obtained under UV and full spectrum illumination.

2.7. Electrochemical impedance spectroscopy (EIS) measurements

The samples were prepared using the same method as in the photocurrent measurements. EIS tests were performed with a frequency loop from 100 kHz to 0.01 Hz by applying a sine wave with an amplitude of 5 mV at open circuit potential. The prepared samples on FTO is used as the photoanode while Pt is used as a counter electrode. The solution medium used is 0.5 M of Na_2SO_4 aqueous solution. The EIS spectra were measured under UV and full spectrum illumination.

3. Results and discussion

The synthesis of modified-TiO_2/Cu (m-TiO_2/Cu) was carried out through a MOF mediated strategy involving three-step process: (i) preparation of modified MIL-125, (ii) Cu precursor loading and (iii) calcination. This photocatalyst has been purposefully designed to capitalize single metal ultrafine Cu clusters supported on MOF-derived metal oxides, capable of achieving non-conflicting structure engineering, enhanced charge transfer dynamics and photothermal effects (Fig. 1). Essentially, m-TiO_2 is designed to exhibit large surface area with hierarchical pore structure that is capable of utilizing the high energy photons (UV), while the ultrafine Cu nanoclusters cocatalyst are responsible for improving the charge transfer dynamics and utilizing lower energy photons (visible-NIR) to synergistically enhance the photocatalytic performance through the photothermal effect. For comparison, a control sample m-TiO_2/Cu-C was also synthesized.

Firstly, in order to obtain a hierarchical porous m-TiO_2, an intentional modification was made to the conventional standard synthesis procedure of the commonly reported MIL-125 [40]. In the solvothermal process, linker deprotonation and metal-linker coordination are initiated by the decomposition of DMF to basic amines at elevated temperatures [41,42]. Reducing the amount of DMF would likely hinder the metal-linker assembly process, ultimately leading to a more defective framework. Thus, through reducing the ratio of DMF to methanol in solution, a modified-MIL-125 (m-MIL-125) can be obtained which exhibits poorer crystallinity and larger pore size as compared to a conventional pristine MIL-125. This is validated through XRD analysis (Fig. S1a) which demonstrates the high crystallinity of MIL-125 similar to those reported in the literature [43–45], while reduced peak intensities were observed for m-MIL-125 indicating poorer crystallinity. The FTIR measurement also demonstrated the reduction in O-Ti-O and C═C bonds in m-MOF, which affirms that the framework is defective (Fig. S1b). In addition, the surface area and pore volume measurements for both samples were carried out using BET (Fig. S2). Although MIL-125 exhibits high surface area of 780 m^2 g^{-1} while that of m-MIL-125 is 240 m^2 g^{-1}, the distinct difference is that MIL-125 consists mainly of micropores, while both micropores and mesopores co-exist in m-MIL-125 (Fig. S2b). Macropores are also observable in the SEM image of m-MIL-125 (Fig. S3a-b), revealing a morphology of highly porous stacked sheet-like structure while Fig. S3c shows MIL-125 to have dense cylinder-like shape. In general, high surface area materials are considered more favorable since they possess sufficient active sites for reactions to take place. However, high surface area material consisting mainly of micropores can also be unfavorable, since the small micropores can greatly restrict the diffusion of reactants/products to the active sites [46,47].

Benefitting from the improved accessibility of reactants due to the hierarchical pore structure, the Cu precursor can be easily incorporated into m-MIL-125 compared to MIL-125. The presence of Cu clusters coordinated sites also serves as a support to prevent structure collapse during calcination. This is evident from the post calcination BET result (Fig. S4a) where the modified MOF derived m-TiO_2/Cu retains a high surface area of 344 m^2 g^{-1}, while retaining both its micropores and mesopores (Fig. S4b). In contrast, the pristine MIL-125 derived TiO_2/Cu, showed a drastic decrease in the amount of its micropores to almost zero. Additionally, the BET results also show a substantial drop in its surface area to 68 m^2 g^{-1} (Fig. S4a), this affirms the structural collapse of TiO_2/Cu, unlike m-TiO_2/Cu that has retained its porous structure (Fig. 1). Similarly, the macropores of m-TiO_2/Cu are also preserved as shown in the SEM image, Fig. 2a. Interestingly, no large Cu particles are observable on the surface of m-TiO_2/Cu under both the SEM (Fig. 2a) and low magnification TEM (Fig. 2b) images, suggesting that the size of the incorporated Cu nanoparticles in m-TiO_2/Cu is extremely small. Multiple HRTEM images (Fig. 2c to Fig. 2e) reveal that the Cu lattice fringe (0.178 nm) which corresponds to the (200) plane, exists in ultrafine clusters. The TEM-EDX mapping (Fig. 2f and Fig. S5-6) confirms that Cu is evenly distributed throughout the sample without the

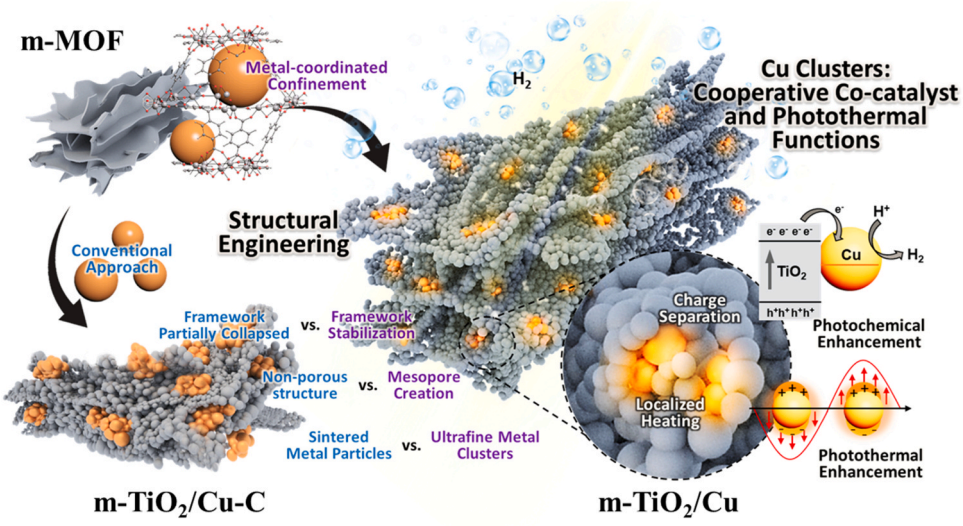

Fig. 1. Schematic diagram of the synthesis process and the structural differences of m-TiO_2/Cu compared with m-TiO_2/Cu-C.

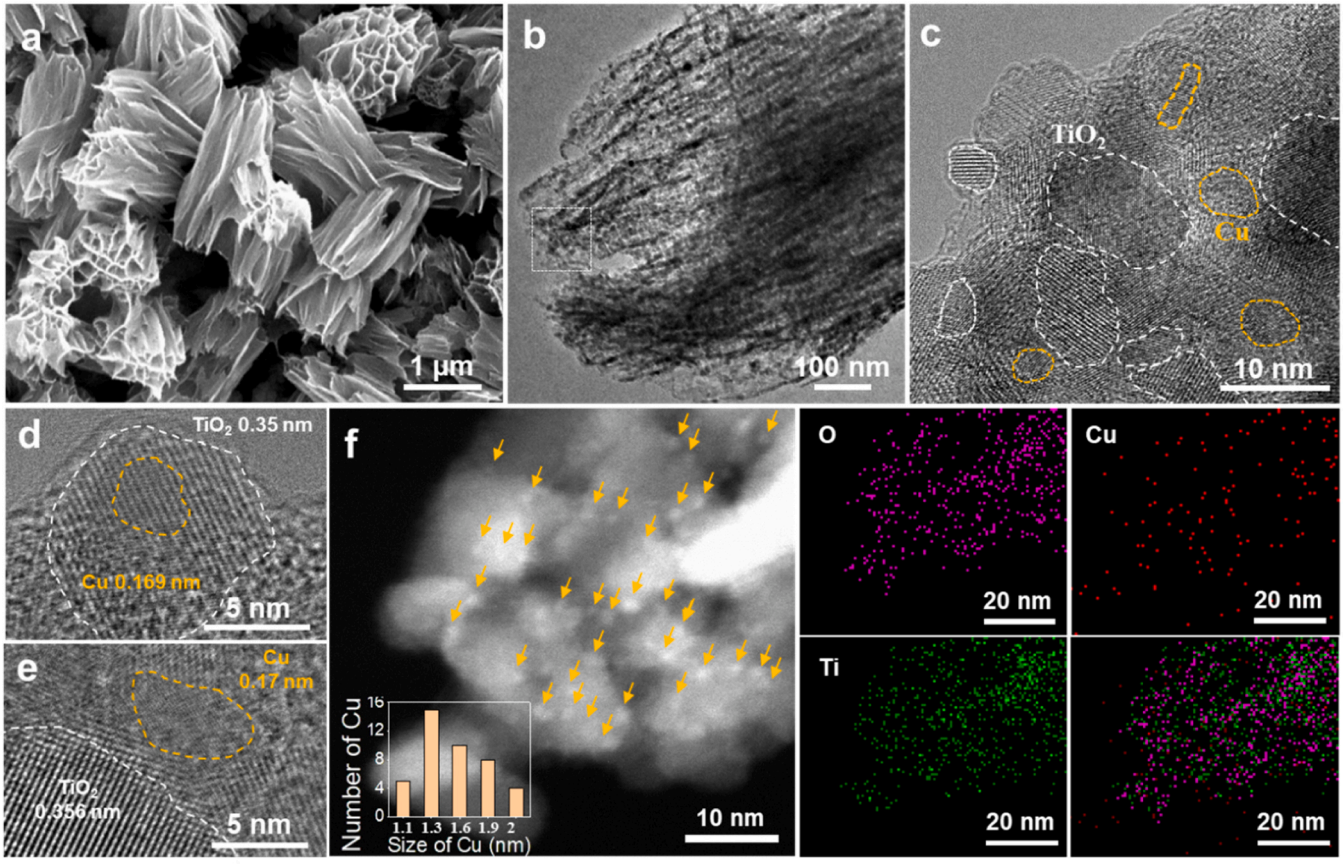

Fig. 2. (a) SEM image, (b) TEM image, (c, d and e) HRTEM images (f) and EDX mapping of m-TiO_2/Cu (inset is a histogram representing the size and number of Cu clusters present in Fig. 2f and Fig. S5).

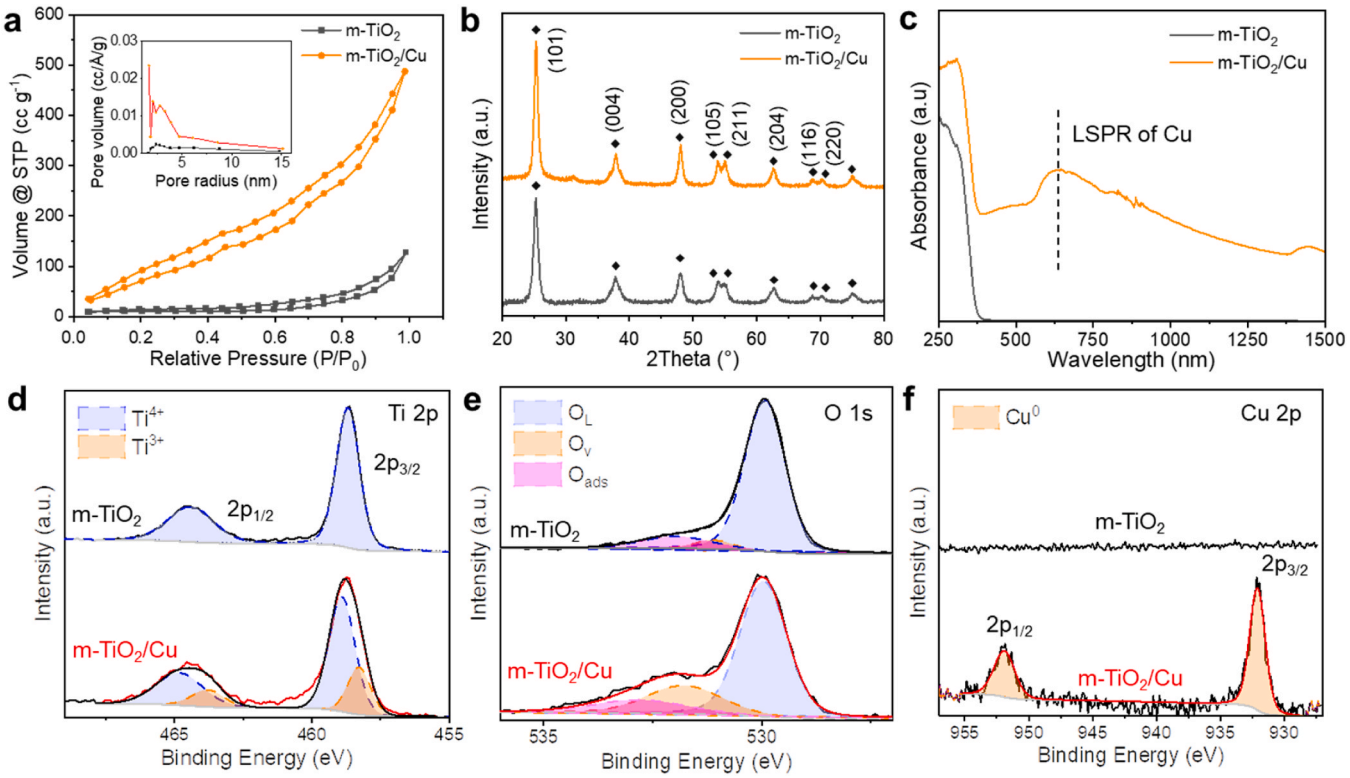

Fig. 3. (a) BET graph and (b) XRD patterns of m-TiO_2 and m-TiO_2/Cu. (c) UV vis spectrum of m-TiO_2 and m-TiO_2/Cu after light irradiation. (d, e and f) XPS spectra of m-TiO_2 and m-TiO_2/Cu.

presence of large Cu particles. From the HAADF TEM image (Fig. 2f and Fig. S5), multiple Cu clusters are identified. A histogram chart was also plotted and the average particle size of the Cu is revealed to be ~ 1.4 nm. This affirms the embeddment of ultrafine dispersed ultrafine Cu nanoclusters within the m-MOF matrix.

As a comparison, m-MIL-125 was also separately calcined without Cu precursor loading to form a control sample, m-TiO_2. Unlike m-TiO_2/Cu that maintains a high surface area post-calcination, m-TiO_2 exhibits a surface area of only 32 m^2 g^{-1} (Fig. 3a), approximately 7.5 times reduction compared to the pre-calcinated m-MIL-125. The porosity of m-TiO_2 is also significantly lower (inset of Fig. 3a), compared to m-TiO_2/Cu, suggesting the collapse of the internal pore structure of m-TiO_2. Overall, these results indicate the vital role Cu plays in preserving the hierarchical porous structure of m-TiO_2/Cu which is crucial for enhancing the photocatalytic activity due to increased accessibility of reactants and active sites. The crystal phases of the samples are confirmed using the XRD as shown in Fig. 3b. Both samples show peaks corresponding to TiO_2 anatase phase (JCPDS No. 78–2486). Peaks relating to Cu metal are not observable in the XRD pattern, which can be attributed to the low loading percentage of Cu in the sample. Nevertheless, apart from HRTEM and TEM-EDX (Fig. 2c to Fig. 2f) that had shown the presence of metallic Cu, its existence can be further validated through complementary techniques such as the UV–vis and XPS. UV–vis absorption spectrum of m-TiO_2 shows an absorption peak in the UV region (Fig. 3c). In addition to this, m-TiO_2/Cu shows a broad peak at ~ 634 nm which is ascribed to the LSPR effect of the ultrafine Cu clusters, induced by the surface oscillations of conduction band electrons [48, 49]. This enhanced light absorption designates that there are more absorbed photons available for conversion into heat. This is extremely beneficial as the heat generated can expedite the holes scavenging process, leading to increased number of electrons available for photocatalytic H_2 generation [50]. Finally, XPS was used to determine the chemical states of the photocatalysts. The XPS scans corroborate the presence of Cu, along with Ti and O species in m-TiO_2/Cu (Fig. 3d to Fig. 3f). A high resolution scan in the Ti 2p region shows a set of doublet peaks which can be attributed to Ti^{4+} at 458.5 and 464.3 eV [51] for both m-TiO_2 and m-TiO_2/Cu samples (Fig. 3d). Interestingly, an additional doublet peaks at 457.9 and 463.6 eV are also observed in m-TiO_2/Cu and can be attributed to Ti^{3+} [52]. The existence of Ti^{3+} suggests the presence of oxygen vacancy, and is in line with the increase in the intensity of O_v peak, observed at 531.6 eV of the O 1 s spectra (Fig. 3e). The presence of such oxygen vacancy has been revealed to be favorable for photocatalytic reactions, as it can help to increase the adsorption of alcohols on the catalyst surface which accelerates the hole scavenging process, and thereby extending the lifetime of the photogenerated electrons [53]. Finally, the Cu species in m-TiO_2/Cu was also confirmed to be metallic in nature, with strong Cu^0 peaks observed without shake up peaks (Fig. 3f).

TiO_2, m-TiO_2 and m-TiO_2/Cu are tested for photocatalytic H_2 generation (Fig. 4a) under UV and full spectrum irradiation to study the unitary effect of structure engineering, charge transfer and photothermal heating. The H_2 production rate of m-TiO_2 under UV irradiation is 1.46 mmol g^{-1} h^{-1}, ~ 5.7 times that of TiO_2 (Fig. S7). Comparing the BET results of m-TiO_2 and TiO_2 (Fig. S8), m-TiO_2 still possesses a higher surface area likely due to the presence of macropores which facilitates reactant diffusion, thus increasing the accessibility of reactants reaching the photocatalyst, resulting in a higher H_2 production rate. Next, the H_2 generation performance of m-TiO_2/Cu synthesized with different amounts of Cu was investigated. Expectedly, the incorporation of ultrafine Cu clusters in TiO_2 results in an enhancement in the H_2 generation rate under UV irradiation. The optimal Cu amount is found to be ~ 4.5%, where the H_2 production rate under UV irradiation is 10.5 mmol g^{-1} h^{-1}, ~ 7.3 times that of m-TiO_2. This increment is ascribed to the lower energy level of Cu, which induces the charge transfer from TiO_2 to Cu. In addition, as a comparison to the current proposed method, a control sample m-TiO_2/Cu-C was also synthesized based on the conventional wet impregnation method to load Cu onto m-TiO_2 [54–56]. The same amount of Cu as the optimized sample was used

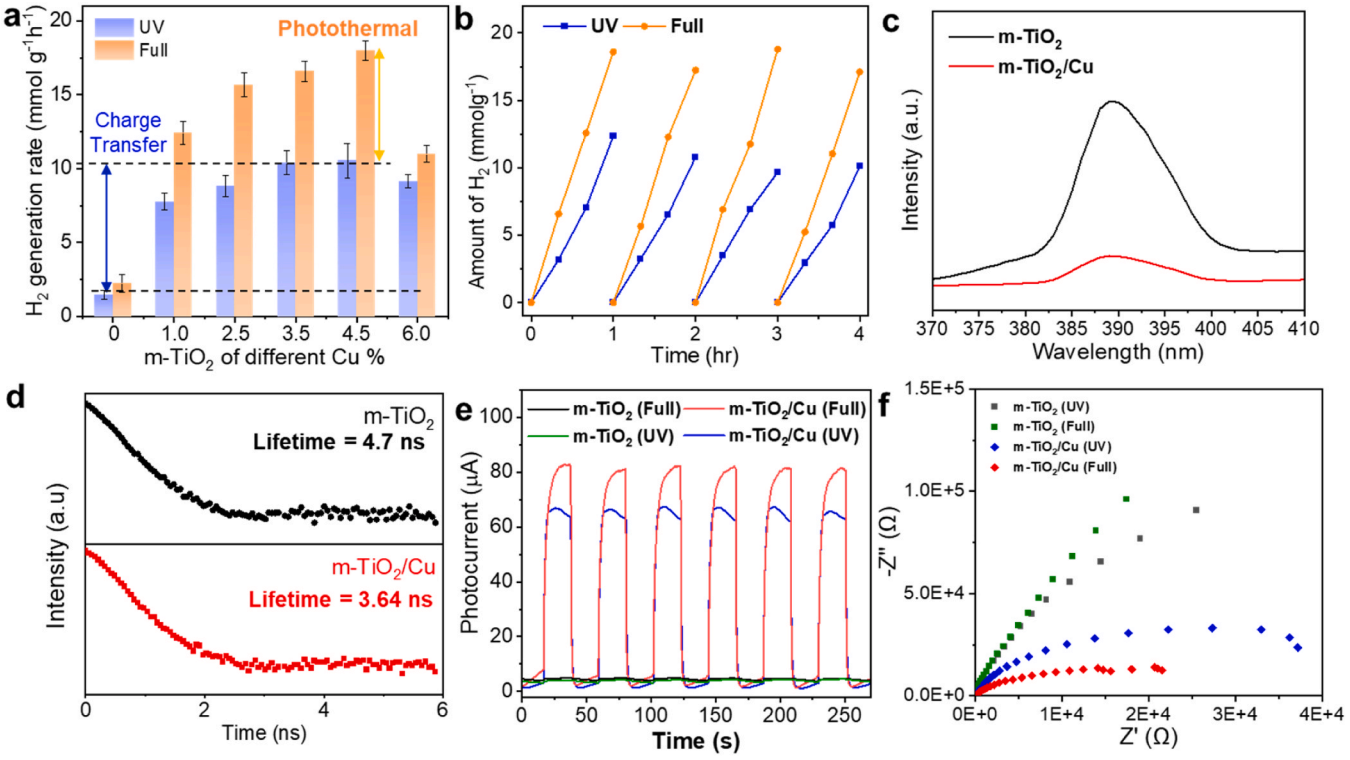

Fig. 4. (a) Hydrogen generation rates of m-TiO_2/Cu at different Cu % concentration under UV and full spectrum irradiation. (b) Hydrogen generation stability of m-TiO_2/Cu. (c, d) Photoluminescence and transient lifetime of m-TiO_2 and m-TiO_2/Cu. (e) Photocurrent and (f) EIS spectrum of m-TiO_2 and m-TiO_2/Cu under UV irradiation and full spectrum irradiation.

for the loading and the presence of Cu, along with Ti and O has been validated through the XPS (Fig. S9). Interestingly, the H_2 generation rate of the optimal sample under UV irradiation is approximately 1 time higher than m-TiO_2/Cu-C (5.1 mmol g^{-1} h^{-1}). This difference can be attributed to the increase in Cu size as seen from the large dark spots in the TEM images (Fig. S10 and Fig. S11). The extraordinary performance of m-TiO_2/Cu can be attributed to the embedment and smaller particle size of Cu where the electron pathway from TiO_2/Cu to the reaction surface is shorten. Furthermore, as the Cu clusters are dispersed uniformly and confined within the pores of m-TiO_2, the agglomeration and out diffusion of the nanoclusters are restricted, ensuring the electron transfer pathway is stable during extended usage of the photocatalyst. This stability is evident from the hydrogen production rate of both m-TiO_2/Cu and m-TiO_2/Cu-C, where m-TiO_2/Cu demonstrated a steady H_2 production rate of 10.5 ± 0.67 (Fig. 4b) while m-TiO_2/Cu-C has an initial rate of 5.1 mmol g^{-1} h^{-1} (Fig. S12) and decreases over repeated cycles.

The photoluminescene (PL) and time-resolved transient PL measurement are carried out to elucidate the charge transfer mechanism. PL arises from the recombination of the photogenerated electron-hole pair and the emission intensity determines the effectiveness of the charge transport from TiO_2 to Cu. The peak intensity weakens upon the addition of Cu as shown in Fig. 4c and this decrease in PL intensity is ascribed to the Cu acting as an electron sink, thereby reducing the charge recombination in TiO_2. It is noteworthy that m-TiO_2/Cu has a lower PL intensity than m-TiO_2/Cu-C (Fig. S13a) which indicates a reduced recombination of charge carriers in m-TiO_2/Cu. This suggests a higher charge transfer efficiency leading to an enhancement in the photocatalytic performance. The suppression of PL implies an accelerated charge transfer process, which leads to a shorter decay lifetime for the photogenerated electrons. To further verify this result, the lifetime measurements are carried out, both m-TiO_2/Cu and m-TiO_2/Cu-C samples exhibit a shorter lifetime than m-TiO_2 as shown in Fig. 4d and Fig. S13b, with m-TiO_2/Cu having the shortest lifetime of 3.64 ns. This is in agreement with the PL measurement, which affirms that m-TiO_2/Cu is indeed more superior than m-TiO_2/Cu-C in preventing charge recombination.

Besides charge transfer efficiency, the photothermal effect of ultrafine Cu clusters on the photocatalytic H_2 generation is also studied. H_2 generation of m-TiO_2/Cu was compared under UV, visible-NIR and full spectrum irradiation (Fig. S14). Interestingly, it could be noted that under only visible-NIR irradiation, negligible amount of hydrogen is produced. However, when visible-NIR irradiation is used in conjunction with UV light (full spectrum), it results in a substantial performance rise as compared to that of under solely UV irradiation. This can be attributed to a visible-NIR irradiation induced photothermal effect of Cu resulting in an enhancement of the photocatalytic performance. The H_2 generation rates of the photocatalyst with different Cu amounts are also measured under UV irradiation and full spectrum irradiation (Fig. 4a). With the incorporation of Cu, the photothermal enhancement remains at ~ 70% with increasing amount of Cu.

Several characterizations, including photocurrent, EIS, temperature profile and KPFM, were employed to affirm the role of Cu for the photothermal enhancement. A higher photocurrent usually suggests easier electrons transport through the electrode and electrolyte. This also indicates a lower charge transfer resistance, leading to a smaller radius observed in the EIS measurement. m-TiO_2/Cu exhibits a higher photocurrent under UV irradiation as compared to m-TiO_2 indicating efficient charge transfer capabilities facilitated by Cu clusters. With the addition of visible-NIR light, the photocurrent of m-TiO_2/Cu increases by ~ 23%, while that of m-TiO_2 increases by only ~8% as shown in Fig. 4e. This is attributed to the photothermal engendered localized temperature increase of plasmonic Cu clusters within m-TiO_2/Cu, which accelerates the scavenging of holes, leading to more available electrons for photoredox reactions, thereby increasing the photocurrent (Fig. S15). The increase in photocurrent is accompanied by the reduction in charge resistance as seen in Fig. 4f. m-TiO_2 demonstrated negligible change in the charge transfer resistance under UV and full spectrum irradiation, which is in agreement with the photocurrent data. In contrast, m-TiO_2/Cu exhibits a significant decrease in charge transfer resistance upon the addition of visible-NIR light. This reduction in charge transfer resistance correlates with the increase in photocurrent as observed in Fig. 4e, thus indicating that the addition of visible-NIR light stimulates more electron generation due to the photothermal effect.

To ascertain the photothermal effect of the Cu cluster in m-TiO_2/Cu, temperature profile measurements of m-TiO_2/Cu and m-TiO_2 under full spectrum illumination are carried out as shown in Fig. 5a. After 25 min of full spectrum irradiation, the temperature of m-TiO_2/Cu reaches around ~ 65.4 °C, while m-TiO_2 reaches ~ 40.1 °C. A difference of ~ 25.3 °C is achieved under full spectrum irradiation, which is ascribed to the heating of the Cu clusters induced by the LSPR effect of Cu. The samples are further studied using KPFM to determine the localized heating effect of ultrafine Cu clusters on the photocatalytic activity under visible-NIR irradiation. As illustrated in the schematic in Fig. 5b, the generation of hot electrons under visible-NIR irradiation will result in an increase in free electrons, causing an upward shift of the Fermi level, reducing the work function. Therefore, determining the light-induced changes in work functions offers an effective technique to visualize the LSPR-induced hot electron generation, which is the source of the localized heating effect. To determine the localized heating effect of ultrafine Cu clusters, KPFM fitted with various light sources was used to investigate the light-induced changes in work function by measuring the variation in contact potential difference (CPD) [57].

$$-\mathrm{CPD} = (\varnothing_{tip} - \varnothing_{sample})/\mathrm{e}$$

where $\varnothing_{tip}$ and $\varnothing_{sample}$ are the work functions of tip and sample, respectively; and e is the electronic charge.

Fig. 5c and Fig. 5d reveal the topography and the mapping of the inverse CPD (-CPD) of m-TiO_2 and m-TiO_2/Cu in dark, visible-NIR (400–1100 nm) and full spectrum irradiation. Under visible-NIR light irradiation, there is negligible variation in the -CPD of m-TiO_2 as compared to dark conditions as seen from the line profiles in Fig. 5e. This is expected as TiO_2 has a large band gap and does not produce electron-hole pairs under visible light irradiation. Upon the addition of UV light, the potential increased by ~ 23 mV. The change in -CPD under UV illumination is ascribed to charge accumulation on the sample surface. This increment arises from the photogenerated electron-hole pairs of TiO_2, which is grounded by Pt coating on the substrate, causing holes to accumulate and result in the increase in -CPD. Next, m-TiO_2/Cu was also irradiated under visible-NIR, and a significant increase in -CPD of ~ 40.1 mV is observed (Fig. 5f). Since TiO_2 is unresponsive under visible light irradiation, the response obtained under visible-NIR can be solely attributed to Cu. According to the above equation, the work function of the tip ($\varnothing_{tip}$) is constant, thus an increase in -CPD suggests a reduction in work function of the sample ($\varnothing_{sample}$), implying an increase in electron density which can be attributed to the LSPR effect of ultrafine Cu clusters under visible-NIR irradiation. This substantiates that hot electrons from Cu are produced in m-TiO_2/Cu which is essential for inducing the photothermal effect. Lastly, when UV light was introduced, an additional increase in -CPD of ~ 50 mV is noted. Given that both photogenerated charge and the LSPR effect would lead to an increase in -CPD, this affirms that there is no conflict between the photothermal and photochemical enhancement of Cu. Therefore, through the use of the KPFM in conjunction with other characterizations and H_2 generation results, the role of ultrafine Cu clusters in m-TiO_2/Cu for both photochemical under UV light irradiation and photothermal enhancement with the implementation of visible-NIR light is verified. It is also important to note that the H_2 generation production rate of m-TiO_2/Cu is ~69 times more than TiO_2 (Fig. S7), which ascertains that Cu indeed aids in preservation of pore structure, charge transfer and photothermal effect.

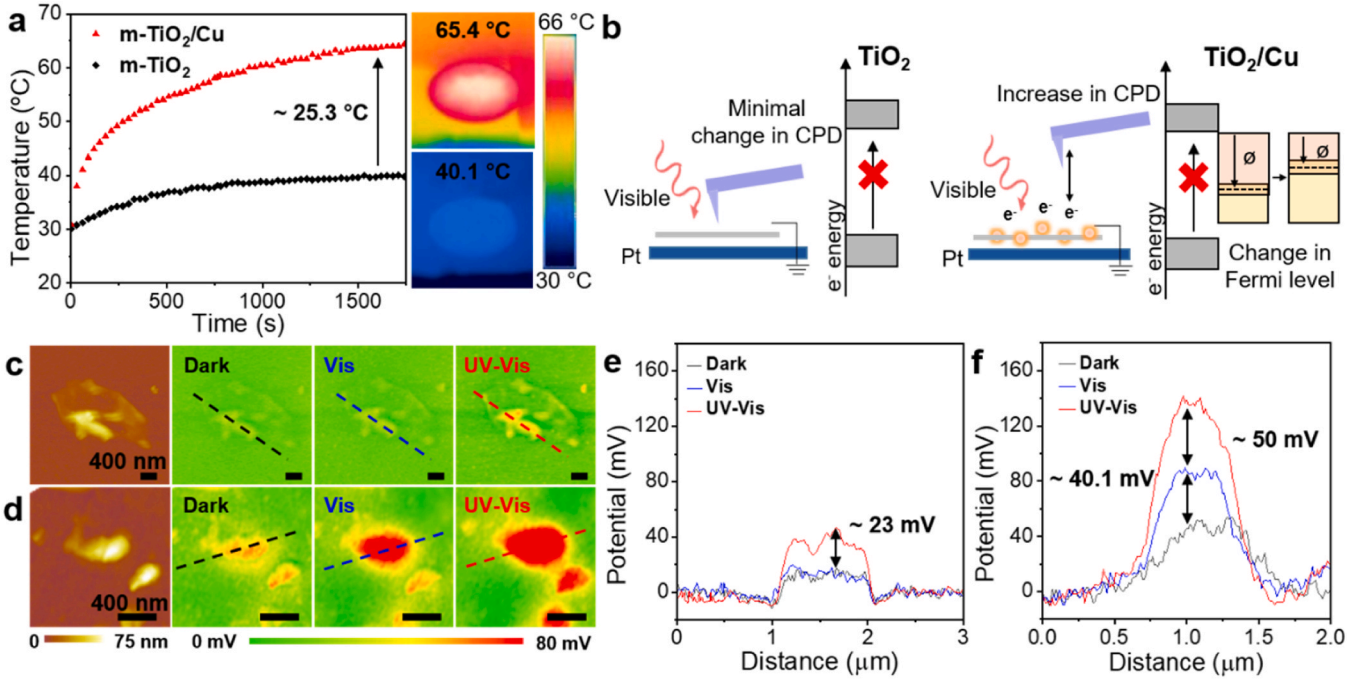

Fig. 5. (a) Temperature profile of m-TiO_2 and m-TiO_2/Cu under full spectrum irradiation. (b) Schematic illustration of the effect of visible-NIR light illumination on the surface potential of m-TiO_2 and m-TiO_2/Cu. (c, d) Topography and the inverse contact potential difference (-CPD) of (c) m-TiO_2 and (d) m-TiO_2/Cu. (e, f) Plot of -CPD against distance along lines indicated in (c, d) under different light source irradiation.

4. Conclusion

The proposed photothermal catalyst design with embedded ultrafine Cu clusters within MOF derived catalyst has shown to overcome challenges related to porous structure collapse, disparate material interfaces and incompatibility between light absorption and charge transfer processes. The photocatalyst (m-TiO_2/Cu) displayed exceptionally high H_2 production rate of 17.9 mmol g^{-1} h^{-1} which is ~69 times that of TiO_2. The hierarchical pore structure facilitates reactant diffusion and increases the interaction of reactants/photocatalyst, leading to an increased number of active sites for H_2 generation. The TiO_2 is set apart for high photon energy utilization, while embedded and uniformly dispersed Cu nanoclusters are used to further enhance the photocatalytic performance through photochemical means. The ultrafine Cu nanocluster also aids in absorbing visible-NIR light for efficient light-to-heat conversion. Notably, the Cu nanoclusters show congruity for both photochemical and photothermal enhancement. The unitary photocatalyst with reinforced porous structure, photochemical and photothermal effect is proven to be achievable. This potentially paves the pathway for the development of other photocatalyst in the field of energy production and sustainability.

CRediT authorship contribution statement

Serene Wen Ling Ng: Conceptualization, Methodology, Investigation, Writing – original draft. **Kane Jian Hong Lim**: Investigation, Writing – review & editing. **Minmin Gao**: Conceptualization, Writing – review & editing. **Wanheng Lu**: Investigation. **Tanmay Ghosh**: Investigation. **Mingsheng Zhang**: Investigation. **Sibudjing Kawi**: Supervision. **Minghui Hong**: Conceptualization, Supervision, Funding acquisition. **Ghim Wei Ho**: Conceptualization, Supervision, Funding acquisition.

Declaration of Competing Interest

The authors declare that they have no known competing financial interests or personal relationships that could have appeared to influence the work reported in this paper.

Data Availability

Data will be made available on request.

Acknowledgements

This research is supported by A*STAR under its 2019 AME IRG & YIRG Grant Calls, A2083c0059 and A*STAR LCERFI project (Award ID: U2102d2011, A-8000278-00-00).

Appendix A. Supporting information

Supplementary data associated with this article can be found in the online version at doi:10.1016/j.apcatb.2023.123182.

References

[1] S. Guo, X. Li, J. Li, B. Wei, Boosting photocatalytic hydrogen production from water by photothermally induced biphase systems, Nat. Commun. 12 (2021) 1343.
[2] X. Yuan, C. Wang, D. Dragoe, P. Beaunier, C. Colbeau-Justin, H. Remita, Highly promoted photocatalytic hydrogen generation by multiple electron transfer pathways, Appl. Catal., B 281 (2021), 119457.
[3] X. Li, S. Zhao, X. Duan, H. Zhang, P. S.-z. Yang, S.P. Zhang, S. Jiang, H. Liu, S. Sun, Wang, Coupling hydrothermal and photothermal single-atom catalysis toward excellent water splitting to hydrogen, Appl. Catal., B 283 (2021), 119660.
[4] H. Lin, S. Luo, H. Zhang, J. Ye, Toward solar-driven carbon recycling, Joule 6 (2022) 294–314.
[5] T.J. Wong, F.J. Lim, M. Gao, G.H. Lee, G.W. Ho, Photocatalytic H_2 production of composite one-dimensional TiO_2 nanostructures of different morphological structures and crystal phases with graphene, Catal. Sci. Technol. 3 (2013) 1086–1093.
[6] W.L. Ong, Y.-F. Lim, J.L. Ting Ong, G.W. Ho, Room temperature sequential ionic deposition (SID) of Ag_2S nanoparticles on TiO_2 hierarchical spheres for enhanced catalytic efficiency, J. Mater. Chem. A 3 (2015) 6509–6516.
[7] T. Kawawaki, Y. Mori, K. Wakamatsu, S. Ozaki, M. Kawachi, S. Hossain, Y. Negishi, Controlled colloidal metal nanoparticles and nanoclusters: recent applications as cocatalysts for improving photocatalytic water-splitting activity, J. Mater. Chem. A 8 (2020) 16081–16113.

[8] W. Kurashige, Y. Niihori, S. Sharma, Y. Negishi, Precise synthesis, functionalization and application of thiolate-protected gold clusters, Coord. Chem. Rev. 320–321 (2016) 238–250.

[9] N. Sakamoto, H. Ohtsuka, T. Ikeda, K. Maeda, D. Lu, M. Kanehara, K. Teramura, T. Teranishi, K. Domen, Highly dispersed noble-metal/chromia (core/shell) nanoparticles as efficient hydrogen evolution promoters for photocatalytic overall water splitting under visible light, Nanoscale 1 (2009) 106–109.

[10] T. Yoshinaga, M. Saruyama, A. Xiong, Y. Ham, Y. Kuang, R. Niishiro, S. Akiyama, M. Sakamoto, T. Hisatomi, K. Domen, T. Teranishi, Boosting photocatalytic overall water splitting by Co doping into Mn_3O_4 nanoparticles as oxygen evolution cocatalysts, Nanoscale 10 (2018) 10420–10427.

[11] K. Wettergren, A. Hellman, F. Cavalca, V.P. Zhdanov, C. Langhammer, Unravelling the dependence of hydrogen oxidation kinetics on the size of Pt nanoparticles by in operando nanoplasmonic temperature sensing, Nano Lett. 15 (2015) 574–580.

[12] W. Huang, C. Su, C. Zhu, T. Bo, S. Zuo, W. Zhou, Y. Ren, Y. Zhang, J. Zhang, M. Rueping, H. Zhang, Isolated electron trap-induced charge accumulation for efficient photocatalytic hydrogen production, Angew. Chem. Int. Ed. 62 (2023), e202304634.

[13] A. Mondal, N.R. Jana, Surfactant-free, stable noble metal–graphene nanocomposite as high performance electrocatalyst, ACS Catal. 4 (2014) 593–599.

[14] Y. Xia, M. Sayed, L. Zhang, B. Cheng, J. Yu, Single-atom heterogeneous photocatalysts, Chem. Catal. 1 (2021) 1173–1214.

[15] C.-Y. Chang, R. Prado-Rivera, M. Liu, C.-Y. Lai, D.R. Radu, Colloidal synthesis and photocatalytic properties of Cu_3NbS_4 and Cu_3NbSe_4 sulvanite nanocrystals, ACS Nanosci. Au 2 (2022) 440–447.

[16] Y. Mun, S. Lee, A. Cho, S. Kim, J.W. Han, J. Lee, Cu-Pd alloy nanoparticles as highly selective catalysts for efficient electrochemical reduction of CO_2 to CO, Appl. Catal., B 246 (2019) 82–88.

[17] M.R. Axet, K. Philippot, Catalysis with colloidal ruthenium nanoparticles, Chem. Rev. 120 (2020) 1085–1145.

[18] K. Chang, H. Pang, X. Hai, G. Zhao, H. Zhang, L. Shi, F. Ichihara, J. Ye, Ultra-small freestanding amorphous molybdenum sulfide colloidal nanodots for highly efficient photocatalytic hydrogen evolution reaction, Appl. Catal., B 232 (2018) 446–453.

[19] T.-H. Yang, Y. Shi, A. Janssen, Y. Xia, Surface capping agents and their roles in shape-controlled synthesis of colloidal metal nanocrystals, Angew. Chem. Int. Ed. 59 (2020) 15378–15401.

[20] Z. Niu, Y. Li, Removal and utilization of capping agents in nanocatalysis, Chem. Mater. 26 (2014) 72–83.

[21] C.M. Phan, H.M. Nguyen, Role of capping agent in wet synthesis of nanoparticles, J. Phys. Chem. A 121 (2017) 3213–3219.

[22] X. Ma, H. Liu, W. Yang, G. Mao, L. Zheng, H.-L. Jiang, Modulating coordination environment of single-atom catalysts and their proximity to photosensitive units for boosting MOF photocatalysis, J. Am. Chem. Soc. 143 (2021) 12220–12229.

[23] A.M. Abdel-Mageed, B. Rungtaweevoranit, M. Parlinska-Wojtan, X. Pei, O. M. Yaghi, R.J. Behm, Highly active and stable single-atom Cu catalysts supported by a metal–organic framework, J. Am. Chem. Soc. 141 (2019) 5201–5210.

[24] Y.-C. Hao, L.-W. Chen, J. Li, Y. Guo, X. Su, M. Shu, Q. Zhang, W.-Y. Gao, S. Li, Z.-L. Yu, L. Gu, X. Feng, A.-X. Yin, R. Si, Y.-W. Zhang, B. Wang, C.-H. Yan, Metal-organic framework membranes with single-atomic centers for photocatalytic CO_2 and O_2 reduction, Nat. Commun. 12 (2021) 2682.

[25] Z. Liu, Z. Chen, M. Li, J. Li, W. Zhuang, X. Yang, S. Wu, J. Zhang, Construction of single Ni atom-immobilized ZIF-8 with ordered hierarchical pore structures for selective CO_2 photoreduction, ACS Catal. (2023) 6630–6640.

[26] Z. Meng, S. Cai, R. Wang, H. Tang, S. Song, P. Tsiakaras, Bimetallic−organic framework-derived hierarchically porous Co-Zn-N-C as efficient catalyst for acidic oxygen reduction reaction, Appl. Catal., B 244 (2019) 120–127.

[27] X. Fang, Q. Shang, Y. Wang, L. Jiao, T. Yao, Y. Li, Q. Zhang, Y. Luo, H.-L. Jiang, Single Pt atoms confined into a metal–organic framework for efficient photocatalysis, Adv. Mater. 30 (2018) 1705112.

[28] A. Arenas-Vivo, S. Rojas, I. Ocaña, A. Torres, M. Liras, F. Salles, D. Arenas-Esteban, S. Bals, D. Ávila, P. Horcajada, Ultrafast reproducible synthesis of a Ag-nanocluster@MOF composite and its superior visible-photocatalytic activity in batch and in continuous flow, J. Mater. Chem. A 9 (2021) 15704–15713.

[29] L. Luo, R. Jin, Atomically precise metal nanoclusters meet metal-organic frameworks, iScience 24 (2021), 103206.

[30] H. Zhang, M. Huang, J. Wen, Y. Li, A. Li, L. Zhang, A.M. Ali, Y. Li, Sub-3 nm Rh nanoclusters confined within a metal–organic framework for enhanced hydrogen generation, Chem. Commun. 55 (2019) 4699–4702.

[31] W. Xu, W. Li, H. Wen, J. Ding, Y. Liu, W. Li, B. Li, Metal/metal-organic framework interfacial ensemble-induced dual site catalysis towards hydrogen generation, Appl. Catal., B 286 (2021), 119946.

[32] M.-L. Xu, J.-D. Cui, J.-H. Zhao, F.-T. Liu, K. Li, Enhanced photocatalytic H_2 production of cadmium-free rGO-mediated ZnS/CuS heterojunction derived from a MOF, CrystEngComm 20 (2018) 5490–5495.

[33] M.Z. Hussain, B. van der Linden, Z. Yang, Q. Jia, H. Chang, R.A. Fischer, F. Kapteijn, Y. Zhu, Y. Xia, Bimetal–organic framework derived multi-heterostructured $TiO_2/Cu_xO/C$ nanocomposites with superior photocatalytic H_2 generation performance, J. Mater. Chem. A 9 (2021) 4103–4116.

[34] Y. Zhang, J. Zhao, H. Wang, B. Xiao, W. Zhang, X. Zhao, T. Lv, M. Thangamuthu, J. Zhang, Y. Guo, J. Ma, L. Lin, J. Tang, R. Huang, Q. Liu, Single-atom Cu anchored catalysts for photocatalytic renewable H_2 production with a quantum efficiency of 56%, Nat. Commun. 13 (2022) 58.

[35] B. Yan, D. Liu, X. Feng, M. Shao, Y. Zhang, Ru species supported on MOF-derived N-doped TiO_2/C hybrids as efficient electrocatalytic/photocatalytic hydrogen evolution reaction catalysts, Adv. Funct. Mater. 30 (2020), 2003007.

[36] X. Xie, L. Peng, H. Yang, G.I.N. Waterhouse, L. Shang, T. Zhang, MIL-101-derived mesoporous carbon supporting highly exposed Fe single-atom sites as efficient oxygen reduction reaction catalysts, Adv. Mater. 33 (2021), 2101038.

[37] H. Zhang, T. Wang, J. Wang, H. Liu, T.D. Dao, M. Li, G. Liu, X. Meng, K. Chang, L. Shi, T. Nagao, J. Ye, Surface-plasmon-enhanced photodriven CO_2 reduction catalyzed by metal–organic-framework-derived iron nanoparticles encapsulated by ultrathin carbon layers, Adv. Mater. 28 (2016) 3703–3710.

[38] M. Gao, C.K. Peh, L. Zhu, G. Yilmaz, G.W. Ho, Photothermal catalytic gel featuring spectral and thermal management for parallel freshwater and hydrogen production, Adv. Energy Mater. 10 (2020) 2000925.

[39] S.W.L. Ng, M. Gao, W. Lu, M. Hong, G.W. Ho, Selective wavelength enhanced photochemical and photothermal H_2 generation of classical oxide supported metal catalyst, Adv. Funct. Mater. 31 (2021) 2104750.

[40] Z. Liu, C. Wang, Y. Wu, L. Geng, X. Zhang, D. Zhang, H. Hu, Y. Zhang, X. Li, W. Liu, P. Na, Synthesis of uniform-sized and microporous MIL-125(Ti) to boost arsenic removal by chemical adsorption, Polyhedron 196 (2021), 114980.

[41] R.S. Forgan, Modulated self-assembly of metal–organic frameworks, Chem. Sci. 11 (2020) 4546–4562.

[42] K.O. Kirlikovali, S.L. Hanna, F.A. Son, O.K. Farha, Back to the basics: developing advanced metal–organic frameworks using fundamental chemistry concepts, ACS Nanosci. Au 3 (2023) 37–45.

[43] X. Zhang, K. Yue, R. Rao, J. Chen, Q. Liu, Y. Yang, F. Bi, Y. Wang, J. Xu, N. Liu, Synthesis of acidic MIL-125 from plastic waste: Significant contribution of N orbital for efficient photocatalytic degradation of chlorobenzene and toluene, Appl. Catal., B 310 (2022), 121300.

[44] H. Wang, X. Yuan, Y. Wu, G. Zeng, H. Dong, X. Chen, L. Leng, Z. Wu, L. Peng, In situ synthesis of In_2S_3@MIL-125(Ti) core–shell microparticle for the removal of tetracycline from wastewater by integrated adsorption and visible-light-driven photocatalysis, Appl. Catal., B 186 (2016) 19–29.

[45] J. Jin, J.P. Kim, S. Wan, K.H. Kim, Y. Choi, P. Li, J. Kang, Z. Ma, J.H. Lee, O. Kwon, D.W. Kim, J.H. Park, Hierarchical pore enhanced adsorption and photocatalytic performance of graphene oxide/Ti-based metal-organic framework hybrid for toluene removal, Appl. Catal., B 317 (2022), 121751.

[46] S. Naghdi, A. Cherevan, A. Giesriegl, R. Guillet-Nicolas, S. Biswas, T. Gupta, J. Wang, T. Haunold, B.C. Bayer, G. Rupprechter, M.C. Toroker, F. Kleitz, D. Eder, Selective ligand removal to improve accessibility of active sites in hierarchical MOFs for heterogeneous photocatalysis, Nat. Commun. 13 (2022) 282.

[47] S.W.L. Ng, G. Yilmaz, W.L. Ong, G.W. Ho, One-step activation towards spontaneous etching of hollow and hierarchical porous carbon nanospheres for enhanced pollutant adsorption and energy storage, Appl. Catal., B 220 (2018) 533–541.

[48] Y. Fang, Z. Cheng, S. Wang, H. Hao, L. Li, S. Zhao, X. Chu, R. Zhu, Effects of oxidation on the localized surface plasmon resonance of Cu nanoparticles fabricated via vacuum coating, Vacuum 184 (2021), 109965.

[49] S. Linic, P. Christopher, D.B. Ingram, Plasmonic-metal nanostructures for efficient conversion of solar to chemical energy, Nat. Mater. 10 (2011) 911–921.

[50] M.-Q. Yang, C.F. Tan, W. Lu, K. Zeng, G.W. Ho, Spectrum tailored defective 2D semiconductor nanosheets aerogel for full-spectrum-driven photothermal water evaporation and photochemical degradation, Adv. Funct. Mater. 30 (2020) 2004460.

[51] Q.-Y. Liu, H.-D. Wang, R. Tang, Q. Cheng, Y.-J. Yuan, Rutile TiO_2 nanoparticles with oxygen vacancy for photocatalytic nitrogen fixation, ACS Appl. Nano Mater. 4 (2021) 8674–8679.

[52] X. Liu, G. Du, M. Li, True photoreactivity origin of Ti^{3+}-doped anatase TiO_2 crystals with respectively dominated exposed {001}, {101}, and {100} facets, ACS Omega 4 (2019) 14902–14912.

[53] X. Pan, M.-Q. Yang, X. Fu, N. Zhang, Y.-J. Xu, Defective TiO_2 with oxygen vacancies: synthesis, properties and photocatalytic applications, Nanoscale 5 (2013) 3601–3614.

[54] S.W.L. Ng, M. Gao, W.L. Ong, K.J.H. Lim, C.K.N. Peh, G.W. Ho, Simultaneous in situ reduction and embedment of Cu nanoparticles into TiO_2 for the design of exceptionally active and stable photocatalysts, J. Mater. Chem. A 6 (2018) 16213–16219.

[55] N. Riaz, F.K. Chong, Z.B. Man, R. Sarwar, U. Farooq, A. Khan, M.S. Khan, Preparation, characterization and application of Cu–Ni/TiO_2 in Orange II photodegradation under visible light: effect of different reaction parameters and optimization, RSC Adv. 6 (2016) 55650–55665.

[56] K.V.R. Chary, G.V. Sagar, D. Naresh, K.K. Seela, B. Sridhar, Characterization and reactivity of copper oxide catalysts supported on TiO_2−ZrO_2, J. Phys. Chem. B 109 (2005) 9437–9444.

[57] W. Melitz, J. Shen, A.C. Kummel, S. Lee, Kelvin probe force microscopy and its application, Surf. Sci. Rep. 66 (2011) 1–27.